

Origin of circular and triangular pores in electron-irradiated hexagonal boron nitride

Umair Javed,^{1,2} Manuel Längle,¹ Vladimír Zobač,¹ Alexander Markevich,¹ Clara Kofler,^{1,2} Martin Paul,¹ Clemens Mangler,¹ Toma Susi,¹ and Jani Kotakoski¹

¹University of Vienna, Faculty of Physics, Boltzmannngasse 5, 1090 Vienna, Austria

²University of Vienna, Vienna Doctoral School in Physics, Boltzmannngasse 5, 1090 Vienna, Austria

For nearly two decades, it has been known that electron irradiation of hexagonal boron nitride (hBN) in a transmission electron microscope leads to the formation of triangular pores. This has been attributed to the lower displacement threshold energy of boron, with or without the assistance of an inelastic scattering event, typically assuming that chemical etching caused by residual gases can be neglected. In this study, in contrast to previous high-vacuum experiments, we show that electron irradiation in ultra-high vacuum leads to circular pores, whereas even small amounts of oxygen in the atmosphere during the experiment change the pores into triangles. *Ab initio* calculations show that oxygen atoms preferentially attach to boron at the pore edge, supporting the hypothesis that they are preferentially etched during irradiation, resulting in nitrogen-terminated triangular defects. Our results explain the origin of triangular pores in hBN and demonstrate a deterministic way to create atomically-defined pores into 2D materials.

INTRODUCTION

Two-dimensional (2D) hexagonal boron nitride (hBN), a wide-bandgap semiconductor with a honeycomb structure of alternating B and N atoms, is an excellent candidate for many applications, such as an electrocatalyst for oxygen evolution reaction [1], as host of quantum emitters [2], as membrane for DNA sequencing [3], and as an active component in energy conversion and storage technologies [4]. Many of the potential applications depend on defect engineering, including creating pores in the material, and a significant effort has been made to understand both defect formation and pore growth in hBN [5, 6]. Transmission electron microscopy (TEM) is an important tool for creating and examining defects in 2D materials [7, 8], where an extended exposure to the electron beam can lead to pore formation [9]. Unlike in an excellent conductor such as graphene [10, 11], in insulators such as hBN, electron irradiation damage is a combination of elastic and inelastic interactions [12, 13]. Additionally, even a partial pressure of oxygen as low as 10^{-8} mbar in the microscope column can play a role, especially in pore growth [14–16]. However, the situation for hBN is not clear, since boron nitride nanotubes have been reported to be resistant to oxygen in the presence of an electron beam [17].

Pore formation in hBN under electron irradiation is of particular interest due to their characteristic triangular shape, known for nearly two decades [18–22]. The broadly accepted explanation for this is that boron is easier to displace than nitrogen owing to their different displacement cross sections [13, 23], leading to triangular pores with nitrogen-terminated edges. However, experimental parameters also seem to influence the pore shape. For example, at 1200°C, the formation of hexagonal pores has been reported in contrast to circular pores at around 800°C and triangular pores at room temperature [24]. It was further demonstrated that focusing an

80-keV beam to 10–20 nm leads to pore drilling through multiple layers, while a broader electron beam (and thus a lower local current) causes the pores to grow predominantly in one layer [25]. It was also shown that a 200-keV electron beam is more effective at drilling holes into multilayer hBN as compared to a 60-keV beam [26]. Finally, a recent study by Bui et al. [13] showed that the displacement cross sections for single nitrogen and boron atoms are similar at low electron energies, indicating that there should be no preference for removal of either of the atomic species, at least from a pristine structure.

Here, we systematically study pore growth in monolayer hBN in a low-pressure oxygen atmosphere under electron irradiation. We show that even a slight amount of oxygen leads to an increase in pore growth as compared to ultra-high vacuum (UHV). We also show that whereas pores in UHV are circular, they turn triangular when as little as 10^{-9} mbar of oxygen is introduced, well below the residual vacuum pressure in typical TEM columns. Besides explaining the formation of triangular pores reported in the literature, our results suggest a route towards atomically precise engineering of pore shapes in hBN.

RESULTS AND DISCUSSION

Commercially available hBN grown via chemical vapor deposition (CVD) from Graphene Supermarket was transferred onto a QuantifoilTM TEM Au grid with 2 μ m diameter holes, as in Ref. [27]. Prior to insertion into the microscope, the samples were baked at ca. 150°C for ca. 12 h in vacuum. The modified Nion UltraSTEM 100 in Vienna [28], an aberration-corrected scanning transmission electron microscopy (STEM) instrument, was used for the experiments. Images were recorded with the medium-angle annular dark-field (MAADF) detector. The base pressure in the sample chamber is in the or-

der of 10^{-10} mbar, and atomic-resolution imaging can be maintained to up to a pressure of ca. 4×10^{-6} mbar [14]. Acceleration voltages of 60 kV and 80 kV were used for imaging.

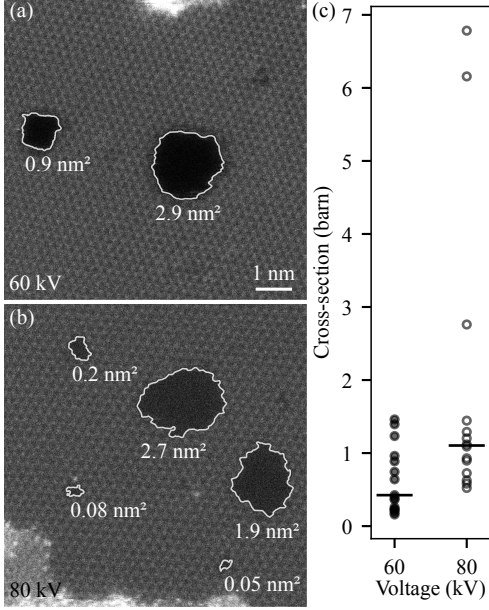


FIG. 1. (a) STEM-MAADF image of round pores in hBN imaged at 60 kV. The pores are highlighted using semi-automatic image analysis. The white lines show the approximate circumferences of each pore, with their areas denoted below. (b) STEM-MAADF image of pores recorded at 80 kV. (c) Displacement cross-section of edge atoms at 60 kV and 80 kV. Each symbol corresponds to one image sequence, and the horizontal line segment denotes the median of each data set.

The effect of prolonged imaging at 60 kV is shown in Fig. 1(a). When hBN is imaged continuously in UHV at 60 kV, defects emerge [13] and grow into pores. However, no preference for either boron- or nitrogen-terminated edges is seen, and the pores appear round or slightly hexagonal, in contrast to other reported room-temperature experiments [18–22, 24, 25, 29–31]. To ensure that this is not due to the lower acceleration voltage, as most of the previous studies were conducted at 80 kV or higher [20, 23, 25], we repeated the experiment at 80 kV (Fig. 1(b)). This resulted in similar pore shapes, but the pores grow faster at the higher voltage (with respect to the electron fluence).

To quantify the pore growth, we estimate the displacement cross-section for edge atoms at both voltages. Since all created pores are circular in shape, we assume that nitrogen and boron atoms at the edge are removed at roughly the same rate and therefore must have similar cross-sections. The pore area (A) is measured semi-automatically via intensity thresholding. In Fig. 1(a, b), we show the pore areas and pore contours overlaid on the original images. The number of atoms ejected N_{ejected} in

each frame was estimated as

$$N_{\text{ejected}} = \frac{\Delta A}{A_{\text{atom}}}, \quad (1)$$

where ΔA is the difference between areas of the pores in subsequent frames and A_{atom} is the area of an individual atom in hBN corresponding to half of the unit cell (ca. 0.0272 nm^2). The number of edge atoms N_{edge} was approximated as

$$N_{\text{edge}} = \frac{\sqrt{4\pi \times A}}{a}, \quad (2)$$

assuming a circular shape for the pores and that each atom occupies a length of a , the lattice parameter of hBN (0.251 nm), along the circumference. This corresponds to assuming a circular shape and that one atom occupies a length of a along the circumference. The displacement cross-section σ for the edge atoms was then calculated as

$$\sigma = \frac{N_{\text{ejected}}}{N_{\text{edge}}} \frac{1}{\phi}, \quad (3)$$

where ϕ is the electron fluence (number of electrons per unit area per frame). For the analysis, only pores with sizes over 0.5 nm^2 were considered. The estimated cross-sections are shown in Fig. 1(c). Despite the obvious uncertainties inherent to each estimation, the cross-section at 60 kV is observably lower than that at 80 kV, with the median values of 0.4 barn and 1.1 barn, respectively. From the pristine lattice, the cross-sections for boron atom ejection was reported as 0.023 ± 0.004 barn (60 kV) and 0.095 ± 0.004 barn (80 kV), while for nitrogen these were 0.016 ± 0.001 barn and 0.057 ± 0.004 barn, respectively [13].

Since the triangular pores reported in the literature do not occur in our UHV experiments at either voltage, we look for an explanation elsewhere. Indeed, in earlier work [14, 15], we showed that low amounts of oxygen in the microscope column can, besides causing a cleaning effect in graphene, also determine the structure of its edges [15]. In another study, we showed that monolayer MoTe_2 is also sensitive to oxygen, even in areas close to but not directly under electron exposure [16]. We therefore turn to study the influence of the atmosphere.

In these experiments, the sample was exposed to different nitrogen and oxygen partial pressures carefully leaked into the column during imaging, as described in Ref. [14]. We note that all pressure values given in this study correspond to the readings of the objective area gauge. However, based on our earlier study [14], the actual pressure at the sample is around an order of magnitude higher than this, which we take into account in all calculations for impingement rates. Comparing the pore growth at different pressures and both acceleration voltages shown in Fig. 2(a), we see a clear increase in the rate of pore growth with an increase in the oxygen partial pressure.

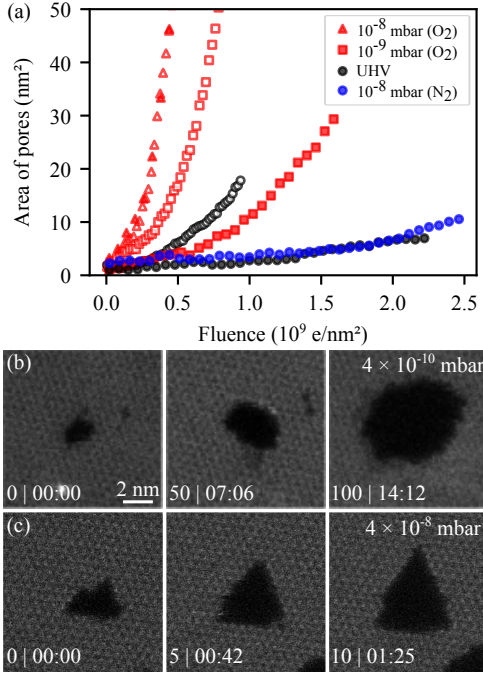


FIG. 2. (a) Pore growth rate for different acceleration voltages and atmospheres. Open symbols represent data recorded at 80 kV whereas filled ones represent 60 kV. (b) Series of cropped STEM-MAADF images of pore growth at 4×10^{-10} mbar. The frame number and the total time (min:s) is noted on the bottom-left corner. (c) Series of cropped STEM-MAADF images of pore growth at 4×10^{-8} mbar oxygen. All original images were recorded with 1024×1024 pixels, at a nominal field of view of 16 nm^2 with $8 \text{ }\mu\text{s}$ dwell time per pixel and $120 \text{ }\mu\text{s}$ flyback time. The uncropped images for both series are shown in the Supplemental Material [32].

In UHV at 80 kV, the rate of the pore growth is higher than at 60 kV (see open vs. filled circles), as already discussed. This is also true at an oxygen pressure of ca. 10^{-9} mbar (open vs. filled rectangles), with the rate of pore growth rising at both voltages compared to UHV. However, at ca. 10^{-8} mbar (open vs. filled triangles), the pore growth rate at both voltages is similar, indicating that the amount of oxygen dominates the process at both voltages. To ensure that this phenomenon is indeed caused by oxygen gas in the column, we repeated the experiment in a nitrogen atmosphere (blue circles). The results are comparable to UHV, demonstrating that nitrogen does not have any effect and confirming that oxygen is the reason for faster pore growth.

Besides the faster pore growth rate, we also observe that the pore shape depends on the oxygen partial pressure. As mentioned, in UHV (Fig. 2(b)), the pores are round. The pore shape remains round when the pressure is increased to ca. 10^{-9} mbar, but at ca. 10^{-8} mbar, pores appear triangular with nitrogen-terminated edges (Fig. 2 (c)).

From these experiments, it is clear that the presence

of even very small amounts of oxygen in the microscope column has a dramatic effect on the pore growth process, changing the pore shape from round to triangular and increasing the pore growth rate. To separate the effect of oxygen from that of the electron beam, the sample was also exposed to oxygen without the beam. Fig. 3(a) shows a ca. $64 \times 64 \text{ nm}^2$ area containing a few pores. After this image was captured, the beam was turned off and oxygen was leaked into the column at a pressure of ca. 10^{-6} mbar. The sample was kept at that pressure for about an hour, and then the leak valve was closed. When the pressure dropped below 10^{-8} mbar, the sample was imaged again. Fig. 3(b) shows that there are practically no changes in the sample due to mere oxygen exposure. Next, the sample was taken out of the vacuum system and kept in an ambient atmosphere (laboratory air) for 11 days, with Fig. 3 (c) recorded afterwards in UHV. The surface contamination has changed because the sample was taken out of the vacuum and heated after insertion; however, the smaller pores have remained practically unchanged, and only minor changes have occurred in the larger pores, presumably due to mechanical stress related to sample handling. This finding is in clear disagreement with Ref. [29], where the authors reported that pores in hBN grew and changed shape after one week of air exposure. In our experiment, oxygen alone had no effect on the sample.

Since the combination of the electron beam with the oxygen partial pressure in the column is responsible for triangular pores, we assume that molecular oxygen, split by the electron beam to atomic oxygen [15], is responsible for the observed changes. To check whether this atomic oxygen leads to pore growth also without electron mediation, we carried out further experiments at an oxygen partial pressure of 4×10^{-9} mbar. At this pressure, pores are usually round. Fig. 4(a) shows an area of $16 \times 16 \text{ nm}^2$ where some pores have already been created by electron irradiation. In the next step, only the middle of the area with a FOV of $8 \times 8 \text{ nm}^2$, shown by the white square, was exposed to the electron beam. Consecutive small frames in Fig. 4(b) show pore growth in that $8 \times 8 \text{ nm}^2$ area. When the initial $16 \times 16 \text{ nm}^2$ area is imaged again after ca. 1 min (Fig. 4 c), we observe round pores in the irradiated smaller FOV. However, outside that area, the pores are triangular and somewhat larger than before. This shows that physical and chemical effects occur simultaneously, with the physical effects dominating inside the irradiated area, resulting in round pores, while outside that area with minimal electron fluence (only exposure due to beam tails) but available atomic oxygen, chemical etching dominates. This indicates that the observed damage in hBN can be quantified as a combination of physical damage caused by the electron beam and chemical damage caused by atomic oxygen. Further, it is possible to tell which type of damage is dominant based on the pore shape.

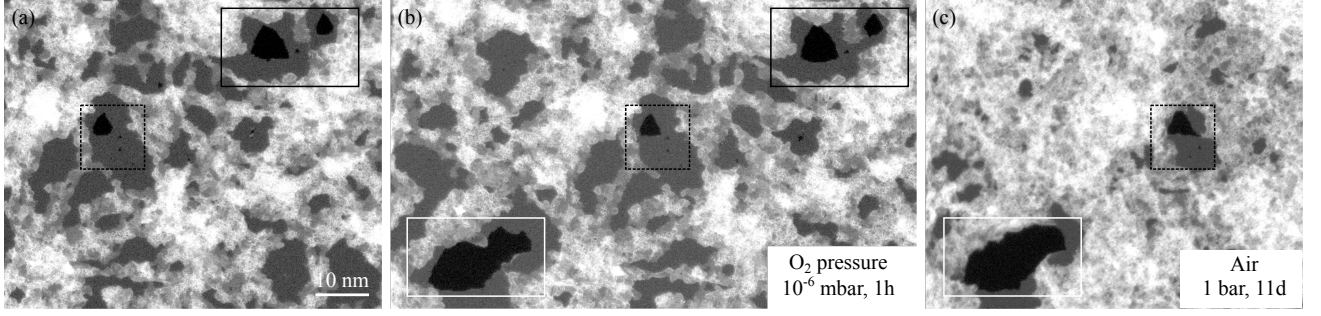


FIG. 3. MAADF-STEM images of (a) hBN with a few pores. (b) The same area after the sample was exposed to oxygen at ca. 10^{-6} mbar pressure for 1 h, without the electron beam (composite of two images near the same field of view). (c) Same sample area after exposure to the ambient atmosphere for 11 days. The same pores are highlighted with corresponding rectangles.

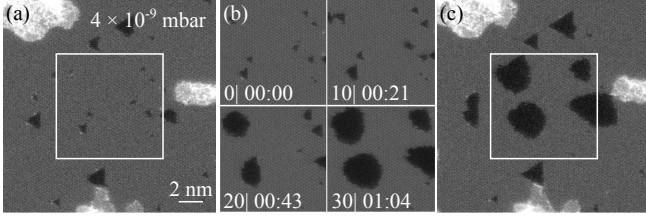


FIG. 4. Pore shape experiment at 4×10^{-9} mbar. (a) A $16 \times 16 \text{ nm}^2$ STEM-MAADF image at the beginning of the experiment. The white square shows the $8 \times 8 \text{ nm}^2$ area which is exposed to the electron beam while recording the image series shown in panel (b). Frame number and frame time are indicated in the bottom-left corners. (c) Image of the initial area of $16 \times 16 \text{ nm}^2$ recorded after the image series.

To quantify this process, we estimate the number of oxygen molecules that are present at the surface at a given pressure using the kinetic theory of gases [33] (with the estimated pressure being one order of magnitude higher than the one shown on the gauge). The rate of impingement in vacuum [34] can be calculated by

$$J = \frac{10 \times P}{\sqrt{2\pi m k_B T}}, \quad (4)$$

where P is the pressure (gauge value multiplied by 10), m is the molecular mass (in the case of the oxygen molecule, 32 amu), k_B is the Boltzmann constant, and T temperature. The impinging rate is multiplied by 2 for two surfaces in the monolayer (bottom and top), the frame time (8.5 s), and area to get the number of impinging molecules per frame (J_{FOV}), or with area per atom (0.0272 nm^2) for the number per atomic site (J_{site}). The impinging rate at different oxygen partial pressures used in this study is shown in the Supplemental Material [32].

The rate of pore growth shown in Fig. 2(a) is quadratic, since, as the pore becomes larger, the number of available atoms at the edges increases. To evaluate in more detail what the exact influence of the oxygen partial pressure is, we performed another set of experiments at 60 kV

to minimize direct electron-beam damage. In these experiments, the pressure is increased slowly, so that in every subsequent measurement, the impingement rate is increased by 0.1 molecules per atomic site per recorded image. At each pressure, several pores were analyzed by estimating the probability of the removal of an edge atom (ρ) through linear regression from N_{ejected} as a function of N_{edge} .

In Fig. 5(a), ρ is plotted as a function of J_{site} . Each data point represents the linear regression comprising all measured pores at the given pressure, with error bars showing the corresponding standard error of the mean. A linear fit to the data yields a slope of 0.52 ± 0.06 removed edge atoms per O_2 molecule; ie. every fourth oxygen atom causes the removal of an atom from the edge.

Our experimental results show that oxygen radicals in the microscope column are responsible for the formation of triangular pores in hBN. However, the mechanism of preferential removal of boron atoms and formation of N-terminated edges remains unclear. To gain more insight into the interaction of oxygen radicals with B and N atoms at the pore edges, we performed plane-wave density functional theory (DFT) simulations. We find that on pristine hBN, an oxygen radical preferably adopts a bridge configuration between B and N atoms, which results in a significant elongation of the B-N bond by $\sim 9.6\%$. Our calculated adsorption energy of -1.89 eV is close to the previously reported value of -2.13 eV [35]. Various configurations of oxygen radicals adsorbed on vacancy defects in hBN with their calculated adsorption energies are shown in Fig. 5(b-d). In particular, we considered single (V_B and V_N , Fig 5b) and double (V_2 , Fig 5c) vacancies, as well as nine-atom vacancies with either N- or B-terminated edges (V_9^N and V_9^B , Fig 5d) to represent small triangular pores. The calculated adsorption energies range from -4.5 to -9.5 eV , indicating strong binding of O radicals to both nitrogen and boron edge atoms. The adsorption energy of the O radical on the N-vacancy is calculated to be -9.30 eV , while for the B-vacancy it

is only -4.54 eV. However, reconstruction of the $V_B:O$ by switching positions of the adjacent N and O atoms leads to a much more favourable configuration ($V_B:O(R)$ in Fig. 5b) with the formation of a B–O–B unit. In the case of double vacancies (Fig. 5c), the B–O–B configuration is 3.7 eV energetically more favourable than N–O–N. Similar trends are observed for the V_9 defects (Fig. 5d): binding of oxygen is stronger on the B-terminated edges. Also, similar to the reconstruction of the $V_B:O$ defect, rotation of the N–O bond in $V_9^N:N-O-N$ structure leads to a lower-energy configuration, although the energy gain is only 0.46 eV.

Overall, our results show that binding of O radicals to boron atoms is energetically much more favourable than binding to nitrogen atoms, with the B–O–B configuration being the most stable. We checked that at least for a double vacancy, this holds true also for ± 1 and ± 2 charge states (Supplemental Material [32]). Interestingly, we also sometimes observe the B–O–B configuration experimentally [32].

To get a more realistic model of experimentally observed pores, we extended the supercell to a size of 8×8 and used the projector-augmented wave DFT method with a linear combination of atomic orbitals (LCAO) basis better suited for larger systems [36]. Two distinct triangular pore types were studied: one with edges terminated by nitrogen atoms and the other with edges terminated by boron atoms, both created by removing 17 atoms.

At the edges, both boron and nitrogen atoms are undercoordinated and seek stabilization by adsorbates, particularly atomic oxygen.

We calculated the adsorption energies and performed nudged elastic band (NEB) simulations to estimate the energy barriers for the desorption of B–O and N–O species and found that adsorption of an oxygen radical on a boron atom releases 8.45 eV, while desorption of the B–O species requires overcoming a barrier of 6.78 eV. By comparison, adsorption on a nitrogen atom releases 5.54 eV, and the desorption of N–O requires overcoming a lower barrier of 2.97 eV.

Although both adsorption processes are exothermic, the stronger thermodynamic driving force is again observed for oxygen adsorption on boron edges. The magnitudes of the desorption energies support the assumption that an electron beam is necessary in addition to the absorption of atomic oxygen to induce pore growth.

While the desorption of N–O is energetically favorable over B–O, the preference of O to bond with B atoms at the edge makes this less likely in practice. We therefore assume that an oxygen atom bonds with boron and forms a molecule consisting of O and B, which is then removed with the assistance of the electron beam, resulting in the formation of N-terminated triangular pores when sufficient O is available. This also agrees with Ref. [37], where TEM-EELS of defective hBN revealed defect peaks that

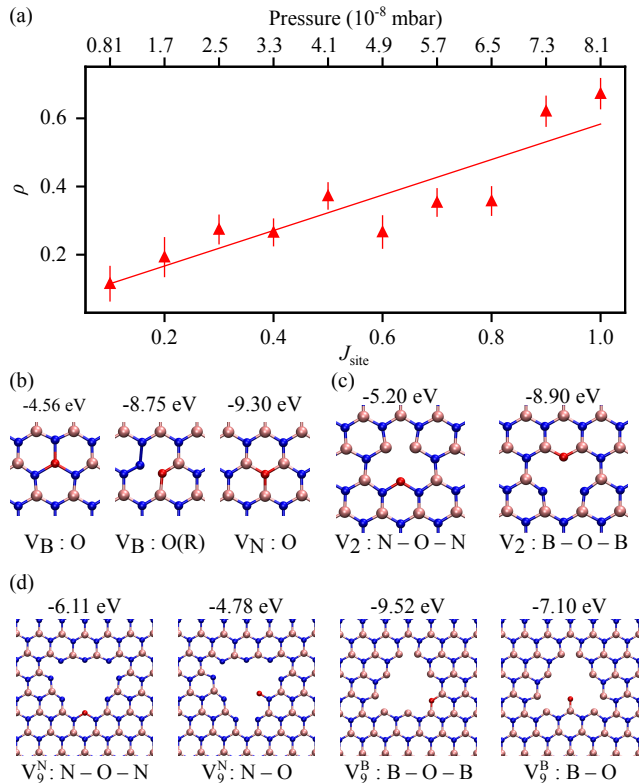


FIG. 5. (a) Probability of removal of an edge atom (ρ) as a function of impinging O_2 molecules per atomic site per recorded image (J_{site}). Atomic structures and DFT calculated absorption energies of oxygen at different configurations of (b) single vacancies, (c) double vacancies, and (d) nitrogen and boron-terminated pores with 9 missing atoms, along with the corresponding atomic structures. Pink spheres represent boron atoms, blue ones nitrogen, and red ones oxygen.

suggest the substitution of nitrogen with oxygen atoms. Interestingly, those peaks were only present when a contaminated area was analyzed, suggesting that molecules consisting of boron and oxygen are removed under the electron beam.

CONCLUSION

We have shown that pore formation in hBN is significantly affected by the presence of oxygen in the microscope column. In UHV (at a pressure of ca. 4×10^{-10} mbar), pore growth in hBN under electron irradiation is significantly slower than at 4×10^{-9} mbar. The pore shape caused by direct electron irradiation in UHV is circular, but becomes triangular under a low-pressure oxygen atmosphere. However, molecular oxygen in itself does not lead to pore growth, as we do not see any changes in the sample in an oxygen atmosphere when the electron beam is off, indicating that the electron beam is required to split oxygen molecules into atomic oxy-

gen. According to our *ab initio* simulations, these oxygen atoms bond preferably with boron atoms at pore edges. Since they are only rarely seen in microscope images, we deduce that the resulting B—O structures are easily removed by the electron beam, leading to nitrogen-terminated triangular pores. Overall, our results demonstrate that pore growth in hBN under electron irradiation is a result of an interplay between knock-on damage and chemical etching by oxygen. Furthermore, the pore shape depends on the dominant process: knock-on damage leads to the formation of round pores, while chemical etching favors triangular nitrogen-terminated pores.

METHODS

Commercially available hBN grown via chemical vapor deposition (CVD) on copper substrate was transferred onto a Quantifoil Au TEM grid (hole diameter 2 μm) by attaching the grid to the hBN/Cu using a drop of isopropanol, and subsequently etching away the substrate in ca. 0.04 M iron(III)-chloride (FeCl_3) solution over 50 h, followed by multiple washing cycles in DI water and isopropanol to remove residual etchant, as described in Ref. [27]. Before insertion into the microscope, the samples were heated in vacuum at around 150°C for ca. 12 h to remove water and contamination from the surface [38].

The Nion UltraSTEM 100 microscope was used for imaging with a medium-angle annular dark-field (MAADF) detector with a semi-angular range of 60–200 mrad. The convergence semi-angle was ca. 35 mrad. The beam current at the 60 kV alignment was around 110–140 pA, and at 80 kV it was around 30–40 pA. The direct-electron detector Dectris ARINA was used to measure the electron dose rate at 80 kV [39]. For 60 keV experiments carried out before the detector was installed, the current was estimated as described in Ref. [40]. Most data was recorded as a stack of images to analyze the rate of pore growth.

The base pressure in the microscope at the sample is around 10^{-10} mbar. Due to modification of the instrument [28], it is possible to leak gas into the column to create a desired atmosphere up to ca. 4×10^{-6} mbar during atomic-resolution imaging [14]. The effect of electron irradiation was measured at a partial pressure range of 10^{-10} – 10^{-8} mbar for oxygen and at a nitrogen partial pressure of ca. 10^{-8} mbar. All pressures reported here are readings of the objective area gauge. In calculations of the impingement rates, a factor of 10 is included (as described in the text) to account for the estimated difference between the actual pressure at the sample and the reading of the gauge [14].

To calculate the rate of pore growth, each image from the stack was analyzed. Pores smaller than 0.5 nm², containing foreign atoms or merging during the measure-

ment, were excluded from the analysis. The area of all pores included in the analysis was calculated and added together as pore area per image. The pores in the images were defined using a threshold, where the dark pixels were contoured to get all the pixels in one pore. The nm/pixel values of the images were calibrated based on the Fast Fourier Transform (FFT) [41], which were then multiplied by the number of pixels in each pore to get their area. Jupyter notebooks were used to analyze the data, and have been made available with the original data [42].

Total-energy density functional theory (DFT) simulations for small vacancy structures were performed using the VASP package [43, 44]. We used the PBE exchange-correlation functional [45] together with the D3 dispersion correction [46]. hBN layers were modelled using hexagonal supercells consisting of 98 atoms with a vacuum layer of 15 Å. The plane-wave energy cutoff was set to 450 eV, and the Brillouin zone was sampled using a $3 \times 3 \times 1$ k -point mesh. Structural relaxation was performed using the conjugate-gradient algorithm with the convergence criterion for the force of 0.01 eV/Å. In all calculations, spin polarization has been taken into account. Adsorption energies were calculated as ($E_{\text{adsorb}} = E_{\text{hBN+O}} - E_{\text{hBN}} - E_{\text{O}}$), where $E_{\text{hBN+O}}$ is the total energy of the defective hBN with the adsorbed oxygen atom, E_{hBN} and E_{O} are the total energies of the defective hBN layer and a separate oxygen atom, respectively.

To perform Nudged elastic band (NEB) simulations, we employed DFT using the GPAW software package [36]. Here, the pristine hBN supercell consisted of an 8×8 supercell containing 128 atoms, while the defective supercell, featuring a pore created by the removal of 17 atoms, contained 111 atoms. The supercell was sufficiently large to allow for k -space sampling using only the Γ point. For all boron and nitrogen atoms, we used a double-zeta polarized (dzp) localized atomic orbital (LCAO) basis set, and a grid spacing of 0.2 Å. Nudged elastic band (NEB) simulations were performed with ten intermediate images to explore the adsorption and dissociation pathways. Also, these calculations were spin-polarized.

ACKNOWLEDGMENTS

This research was funded in part by the Austrian Science Fund (FWF) [10.55776/COE5 and 10.55776/P36264]. For open-access purposes, the author has applied a CC-BY public copyright license to any author-accepted manuscript version arising from this submission.

Author contributions

UJ and JK conceived the study. UJ, CM, ML, CK, and MP conducted the experimental work. UJ, MP, ML, and JK performed the data analysis. CK prepared the samples. VZ and AM performed the *ab initio* calculations. UJ, ML, and JK wrote the manuscript, with contributions from all authors. TS and JK supervised the study.

-
- [1] A. F. Khan, E. P. Randviir, D. A. C. Brownson, X. Ji, G. C. Smith, and C. E. Banks, *Electroanalysis* **29**, 622 (2017).
 - [2] T. T. Tran, K. Bray, M. J. Ford, M. Toth, and I. Aharonovich, *Nature Nanotechnology* **11**, 37 (2016).
 - [3] Z. Zhou, Y. Hu, H. Wang, Z. Xu, W. Wang, X. Bai, X. Shan, and X. Lu, *Scientific Reports* **3**, 3287 (2013).
 - [4] R. Han, F. Liu, X. Wang, M. Huang, W. Li, Y. Yamauchi, X. Sun, and Z. Huang, *Journal of Materials Chemistry A* **8**, 14384 (2020).
 - [5] Q. Weng, X. Wang, X. Wang, Y. Bando, and D. Golberg, *Chemical Society Reviews* **45**, 3989 (2016).
 - [6] D. O. Byrne, S. M. Ribet, D. Kepaptsoglou, Q. M. Ramasse, C. Ophus, and F. I. Allen, "Fabrication and characterization of boron-terminated tetravacancies in monolayer hBN using STEM, EELS and electron ptychography," (2025).
 - [7] S. Su, X. Wang, and J. Xue, *Materials Horizons* **8**, 1390 (2021).
 - [8] J. P. Thiruraman, K. Fujisawa, G. Danda, P. M. Das, T. Zhang, A. Bolotsky, N. Perea-López, A. Nicolaï, P. Senet, M. Terrones, and M. Drndić, *Nano Letters* **18**, 1651 (2018).
 - [9] M. D. Fischbein and M. Drndić, *Applied Physics Letters* **93**, 113107 (2008).
 - [10] T. Susi, C. Hofer, G. Argentero, G. T. Leuthner, T. J. Pennycook, C. Mangler, J. C. Meyer, and J. Kotakoski, *Nature Communications* **7**, 13040 (2016).
 - [11] J. C. Meyer, F. Eder, S. Kurasch, V. Skakalova, J. Kotakoski, H. J. Park, S. Roth, A. Chuvilin, S. Eychen, G. Benner, A. V. Krasheninnikov, and U. Kaiser, *Physical Review Letters* **108**, 196102 (2012).
 - [12] T. Susi, J. C. Meyer, and J. Kotakoski, *Nature Reviews Physics* **1**, 397 (2019).
 - [13] T. A. Bui, G. T. Leuthner, J. Madsen, M. R. A. Monazam, A. I. Chirita, A. Postl, C. Mangler, J. Kotakoski, and T. Susi, *Small* **19**, 2301926 (2023).
 - [14] G. T. Leuthner, S. Hummel, C. Mangler, T. J. Pennycook, T. Susi, J. C. Meyer, and J. Kotakoski, *Ultramicroscopy* **203**, 76 (2019).
 - [15] G. T. Leuthner, T. Susi, C. Mangler, J. C. Meyer, and J. Kotakoski, *2D Materials* **8**, 035023 (2021).
 - [16] E. H. Ahlgren, A. Markevich, S. Scharinger, B. Fickl, G. Zagler, F. Herterich, N. McEvoy, C. Mangler, and J. Kotakoski, *Advanced Materials Interfaces* **9**, 2200987 (2022).
 - [17] H.-Y. Chao, A. M. Nolan, A. T. Hall, D. Golberg, C. Park, W.-C. D. Yang, Y. Mo, R. Sharma, and J. Cummings, *The Journal of Physical Chemistry C* **128**, 18328 (2024).
 - [18] C. Jin, F. Lin, K. Suenaga, and S. Iijima, *Physical Review Letters* **102**, 195505 (2009).
 - [19] G. H. Ryu, H. J. Park, J. Ryou, J. Park, J. Lee, G. Kim, H. S. Shin, C. W. Bielawski, R. S. Ruoff, S. Hong, and Z. Lee, *Nanoscale* **7**, 10600 (2015).
 - [20] J. C. Meyer, A. Chuvilin, G. Algara-Siller, J. Biskupek, and U. Kaiser, *Nano Letters* **9**, 2683 (2009).
 - [21] N. Alem, R. Erni, C. Kisielowski, M. D. Rossell, W. Gannett, and A. Zettl, *Physical Review B* **80**, 155425 (2009).
 - [22] D. O. Byrne and F. I. Allen, *ACS Applied Nano Materials* (2025), 10.1021/acsanm.4c06998.
 - [23] J. Kotakoski, C. H. Jin, O. Lehtinen, K. Suenaga, and A. V. Krasheninnikov, *Physical Review B* **82**, 113404 (2010).
 - [24] O. Cretu, Y.-C. Lin, and K. Suenaga, *Micron* **72**, 21 (2015).
 - [25] S. M. Gilbert, G. Dunn, A. Azizi, T. Pham, B. Shevitski, E. Dimitrov, S. Liu, S. Aloni, and A. Zettl, *Scientific Reports* **7**, 15096 (2017).
 - [26] R. N. Keneipp, J. A. Gusdorff, P. Bhatia, T. T. Shin, L. C. Bassett, and M. Drndić, *The Journal of Physical Chemistry C* **128**, 8741 (2024).
 - [27] M. R. Ahmadpour Monazam, U. Ludacka, H.-P. Komsa, and J. Kotakoski, *Applied Physics Letters* **115**, 071604 (2019).
 - [28] M. Hotz, G. Corbin, N. Dellby, O. Krivanek, C. Mangier, and J. Meyer, *Microscopy and Microanalysis* **22**, 34 (2016).
 - [29] C. Dai, D. Popple, C. Su, J.-H. Park, K. Watanabe, T. Taniguchi, J. Kong, and A. Zettl, *Communications Chemistry* **6**, 1 (2023).
 - [30] L.-C. Yin, H.-M. Cheng, and R. Saito, *Physical Review B* **81**, 153407 (2010).
 - [31] T. Xu, Y. Tu, Y. Zhu, Y. Shen, K. Yin, and L. Sun, *Nanoscale* **14**, 17182 (2022).
 - [32] See Supplemental Material for additional figures regarding larger field of view images of pores at different partial pressures, impingement rate at the different pressures, STEM-MAADF image of an oxygen atom bonded to two boron atoms at the nitrogen site, total energies at different charge states for B-O-B and N-O-N configurations at a double vacancy, adsorption energies for oxygen near the edge of a V_9 defect, and nudged elastic band calculations for oxygen adsorption and desorption at both nitrogen and boron-terminated edges.
 - [33] J. C. Maxwell, *The London, Edinburgh, and Dublin Philosophical Magazine and Journal of Science* (1860), 10.1080/14786446008642818.
 - [34] J. F. O'Hanlon, *A User's Guide to Vacuum Technology*, 3rd ed. (Wiley-Interscience, 2003) accessed: 2025-06-08.
 - [35] Y. Zhao, X. Wu, J. Yang, and X. C. Zeng, *Phys. Chem. Chem. Phys.* **14**, 5545 (2012).
 - [36] J. J. Mortensen, A. H. Larsen, M. Kuisma, A. V. Ivanov, A. Taghizadeh, A. Peterson, A. Haldar, A. O. Dohn, C. Schäfer, E. Ö. Jónsson, E. D. Hermes, F. A. Nilsson, G. Kastlunger, G. Levi, H. Jónsson, H. Häkkinen, J. Fojt, J. Kangsabanik, J. Söderquist, J. Lehtomäki, J. Heske, J. Enkovaara, K. T. Winther, M. Dulak, M. M. Melander, M. Ovesen, M. Louhivuori, M. Walter, M. Gjerding, O. Lopez-Acevedo, P. Erhart, R. Warmbier, R. Würdemann, S. Kaappa, S. Latini, T. M. Boland, T. Bligaard, T. Skovhus, T. Susi, T. Maxson, T. Rossi, X. Chen, Y. L. A. Schmerwitz, J. Schiøtz, T. Olsen, K. W. Jacobsen, and K. S. Thygesen, *The Journal of*

- Chemical Physics **160**, 092503 (2024).
- [37] D. O. Byrne, J. Ciston, and F. I. Allen, *Microscopy and Microanalysis* **30**, 650 (2024).
 - [38] M. Tripathi, A. Mittelberger, K. Mustonen, C. Mangler, J. Kotakoski, J. C. Meyer, and T. Susi, *physica status solidi (RRL) – Rapid Research Letters* **11**, 1700124 (2017).
 - [39] T. Susi, *Journal of Microscopy* (2025), 10.1111/jmi.13409.
 - [40] C. Speckmann, J. Lang, J. Madsen, M. R. A. Monazam, G. Zagler, G. T. Leuthner, N. McEvoy, C. Mangler, T. Susi, and J. Kotakoski, *Physical Review B* **107**, 094112 (2023).
 - [41] J. Madsen, “fourier-scale-calibration,” <https://github.com/jacobjma/fourier-scale-calibration> (2023).
 - [42] U. Javed, M. Längle, V. Zobač, A. Markevich, C. Kofler, M. Paul, C. Mangler, T. Susi, and J. Kotakoski, “Original data ”origin of circular and triangular pores in electron-irradiated hexagonal boron nitride”,” (2025), phaidra ID: o:2144401.
 - [43] G. Kresse and J. Hafner, *Phys. Rev. B* **47**, 558 (1993).
 - [44] G. Kresse and J. Furthmüller, *Computational Materials Science* **6**, 15 (1996).
 - [45] J. P. Perdew, K. Burke, and M. Ernzerhof, *Phys. Rev. Lett.* **77**, 3865 (1996).
 - [46] S. Grimme, S. Ehrlich, and L. Goerigk, *Journal of Computational Chemistry* **32**, 1456 (2011).

Supplemental Material

**Electron-irradiation-induced pore formation in 2D hexagonal boron nitride in
ultra-high vacuum and in a low-pressure O₂ atmosphere**

Umair Javed^{1,2}, Manuel Längle¹, Vladimír Zobač¹, Alexander Markevich¹, Clara Kofler^{1,2}, Martin Paul¹, Clemens Mangler¹, Toma Susi¹, Jani Kotakoski¹

¹ University of Vienna, Faculty of Physics, Boltzmanngasse 5, 1090 Vienna, Austria

² University of Vienna, Vienna Doctoral School in Physics, Boltzmanngasse 5, 1090 Vienna, Austria

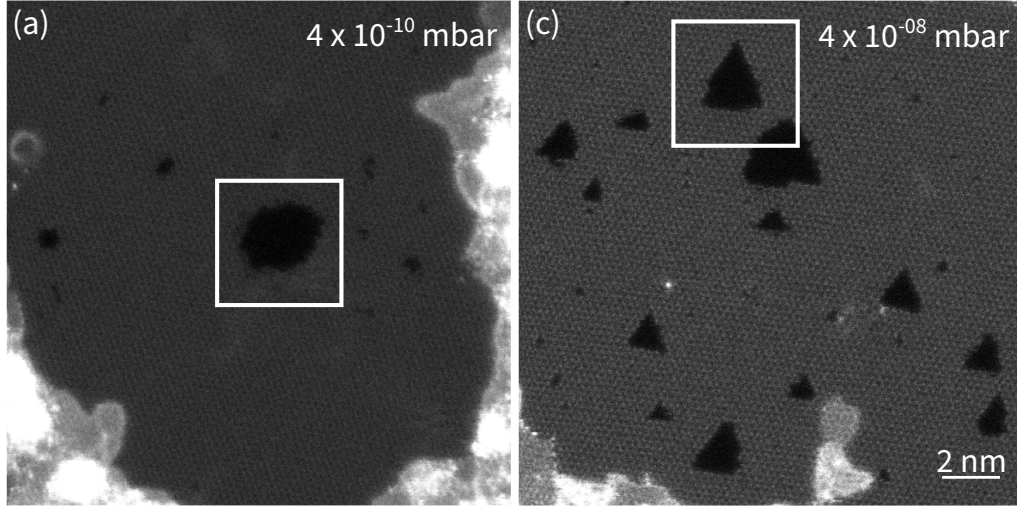


FIG. S1. Overview STEM-MAADF images of the pore growth series in Fig. 2.

TABLE I. Rate of oxygen molecules impinging the surface of the sample within a 16 nm^2 field of view or an atomic site per frame at each partial pressure (site here refers to a lattice site in a pristine hBN structure).

Pressure (mbar)	$J[\text{m}^{-2}\text{s}^{-1}]$	J_{FOV}	J_{Site}
4.5×10^{-9}	1.2×10^{17}	527	0.05
8.1×10^{-9}	2.1×10^{17}	949	0.1
1.7×10^{-8}	4.6×10^{17}	1992	0.2
2.5×10^{-8}	6.8×10^{17}	2929	0.3
3.3×10^{-8}	8.9×10^{17}	3867	0.4
4.1×10^{-8}	1.1×10^{18}	4804	0.5
4.9×10^{-8}	1.3×10^{18}	5742	0.6
5.7×10^{-8}	1.5×10^{18}	6679	0.7
6.5×10^{-8}	1.7×10^{18}	7617	0.8
7.3×10^{-8}	1.9×10^{18}	8554	0.9
8.1×10^{-8}	2.1×10^{18}	9492	1.0

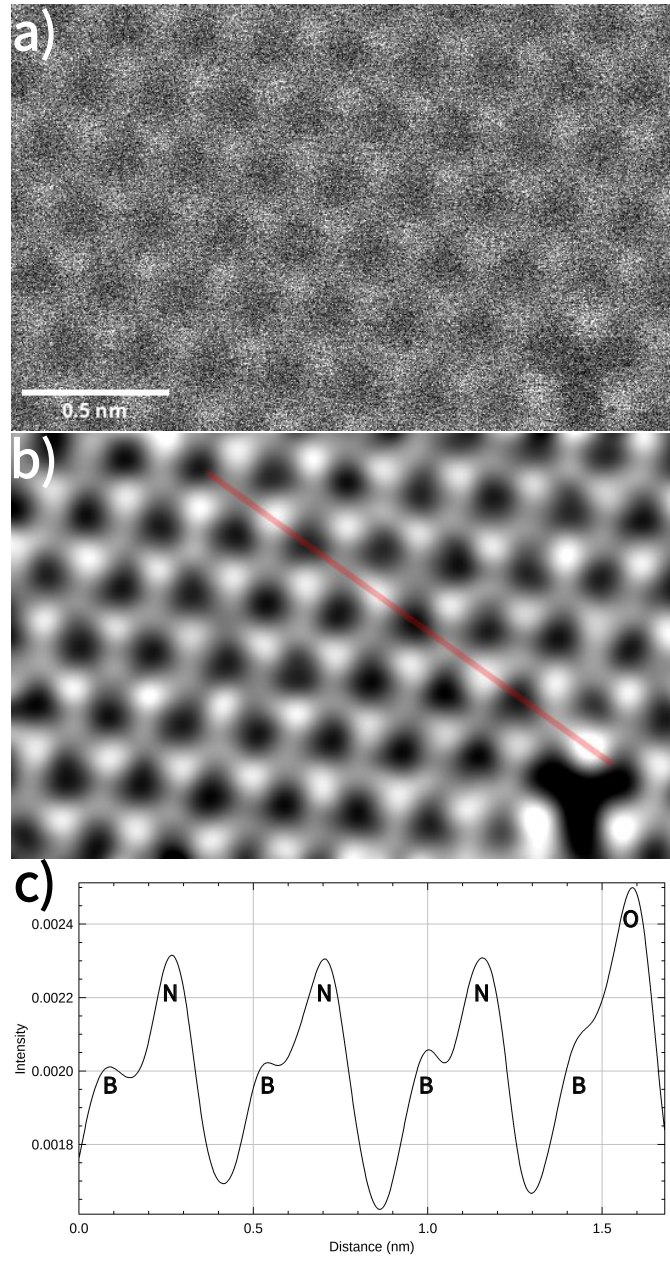


FIG. S2. (a) STEM-MAADF image at the pressure of 5.7×10^{-8} mbar, (b) image with Gaussian filter applied and a line profile, (c) intensity of the line profile.

TABLE II. Calculated total energy difference between B–O–B and N–O–N configurations for different charge states of the double vacancy defect in hBN with an oxygen atom (see the main article for the atomic configurations).

Charge, e^-	ΔE , eV
-1	-6.61
0	-3.70
+1	-3.10
+2	-3.07

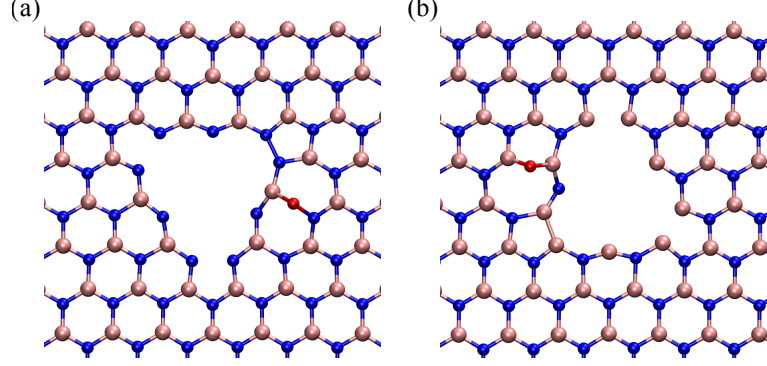


FIG. S3. Adsorption of oxygen on hBN near the edges of V_9 defects. In the case of V_9^N , oxygen radical adsorption on the B–N bond close to the edge leads to breaking of the bond (Fig. 5b), with the distance between B and N atoms becoming ~ 2.5 Å. The adsorption energy is calculated to be -3.94 eV, which is significantly lower compared to the pristine surface. Adsorption of O near the B-terminated edge leads to even more drastic changes in the bonding (Fig. 5c): the N atom is pushed towards the edge and a B–O–B bridge configuration is formed, resulting in the adsorption energy of -6.10 eV. (The desorption energies of N–O and B–O calculated with VASP (from the configurations shown in Figure 5(d) for V_9 defects) are 2.61 eV and 7.28 eV.

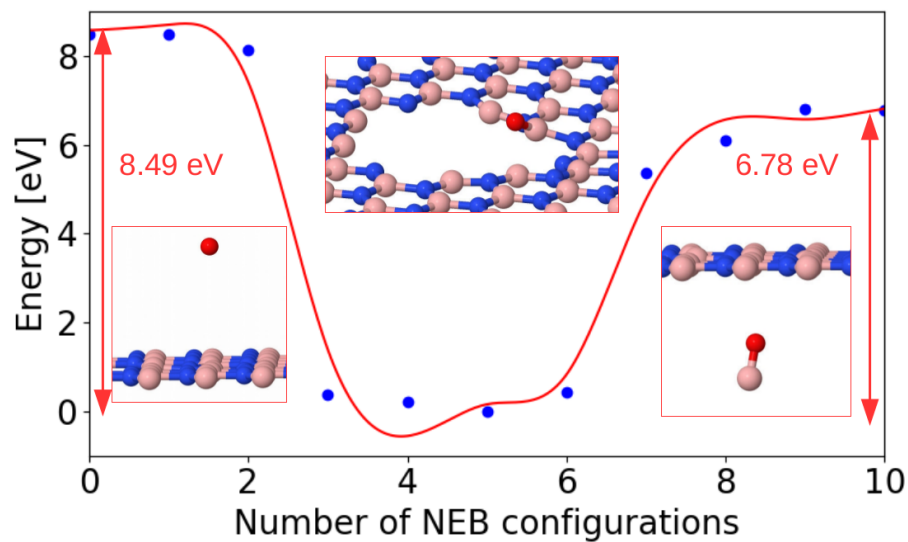


FIG. S4. Energy profile of the oxygen adsorption and desorption process on a boron-terminated edge obtained from NEB simulations. The inset panels depict the initial, intermediate, and final configurations along the reaction path. The red curve serves as a visual guide, generated by spline interpolation of the discrete NEB energy points.

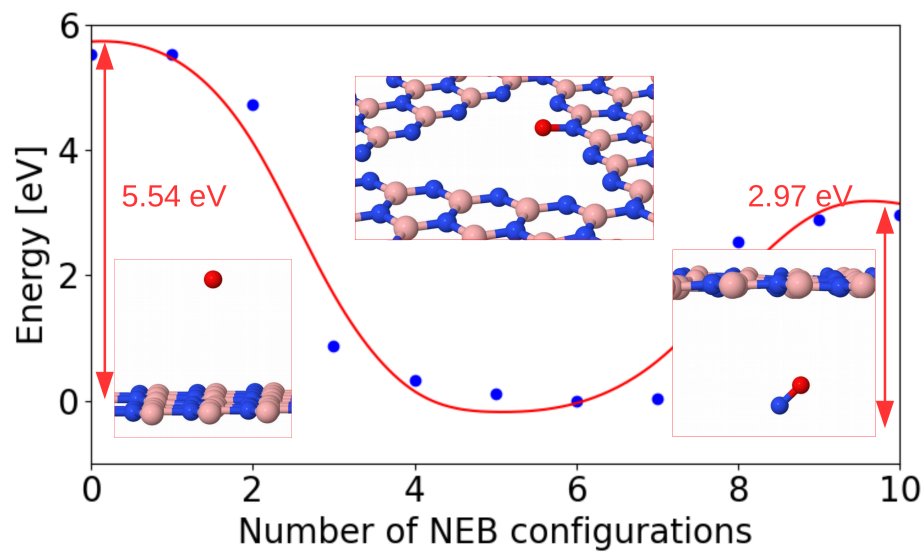


FIG. S5. Energy profile of the oxygen adsorption and desorption process on a nitrogen-terminated edge, obtained from NEB simulations. The inset panels depict the initial, intermediate, and final configurations along the reaction path. The red curve serves as a visual guide, generated by spline interpolation of the discrete NEB energy points.